arXiv:1403.1503v1 [cond-mat.mtrl-sci] 6 Mar 2014

Momentum space anisotropy of electronic correlations in Fe and Ni - an analysis of magnetic Compton profiles

L. Chioncel[a,b], D. Benea[c,a], H. Ebert[d], I. Di Marco[e] and J. Minár[d,f]

[a] *Theoretical Physics III, Center for Electronic Correlations and Magnetism, Institute of Physics, University of Augsburg, D-86135 Augsburg, Germany*

[b] *Augsburg Center for Innovative Technologies, University of Augsburg, D-86135 Augsburg, Germany*

[c] *Faculty of Physics, Babes-Bolyai University, Kogalniceanustr 1, Ro-400084 Cluj-Napoca, Romania*

[d] *Chemistry Department, Munich University, Butenandstr. 5-13, D-81377 München, Germany*

[e] *Department of Physics and Astronomy, Division of Materials Theory, Uppsala University, Box 516, SE-75120 Uppsala, Sweden and*

[f] *New Technologies - Research Center, University of West Bohemia, Univerzitni 8, 306 14 Pilsen, Czech Republic*

Abstract

The total and magnetically resolved Compton profiles are analyzed within the combined density functional and dynamical mean field theory for the transition metal elements Fe and Ni. A rather good agreement between the measured and computed magnetic Compton profiles (MCPs) of Fe and Ni is obtained with the standard Local Spin Density Approximation (LSDA). By including local but dynamic many-body correlations captured by Dynamical Mean Field Theory (DMFT), the calculated magnetic Compton profile is further improved when compared with experiment. The second moment of the difference of the total Compton profiles between LSDA and DMFT, along the same momentum direction, has been used to discuss the strength of electronic correlations in Fe and Ni.

I. INTRODUCTION

The single particle momentum density of an interacting electronic system can be measured rather directly by high energy Compton scattering experiments [1]. These experiments in metals provide direct information about the occupied momentum states and the Fermi surface. Although the momentum density is a relatively simple function it incorporates in a non-trivial way the many-body aspects of the interactions between the electrons of the system.

For several transition metal elements discrepancies between measured and computed Compton profiles are found in the low momentum region (Fe, Ni, V, Cr) [2–7]. The Compton profile represents a directional property of the investigated system, therefore measurements with p_z aligned with various crystallographic directions ($\mathbf{K}$) provide information related to their structure and the Fermi surface through the Compton profile anisotropy. Although the computed anisotropy or difference profile, i.e. the difference between two Compton profiles taken along different directions (for example $\mathbf{K}$=[110] and $\mathbf{K}'$=[100])

$$\Delta J^{struc}(p) = J_{110}(p) - J_{100}(p) \tag{1}$$

has in general a trend similar to the experimental spectra, it often displays larger amplitudes of oscillations in comparison with the measured profiles. The amplitudes of the characteristic oscillations are determined by details of the fine structures of the momentum densities. Therefore, the *structural anisotropies* expressed by Eq. (1) are related to some specific features of the Fermi surface topology. In order to address these discrepancies, Lam and Platzmann [8, 9] introduced a correction related to the difference between the occupation function for a non-interacting electron gas $n^{free}(\mathbf{k})$ and a homogeneous interacting electron gas $n^{int}(\mathbf{k})$. This correction takes the form of:

$$\Delta J^{LP}(p) = \int \rho(\mathbf{r})(J^{int}(p)[\rho] - J^{free}(p)[\rho])d^3\mathbf{r} \tag{2}$$

The Lam-Platzman correction Eq. (2) acts in the low-momentum region and for some cases it reduces the differences between experiment and theory. Nevertheless, the theoretical values still overestimate the amplitude with respect to the experiment in the low momentum region and in addition the residual differences appear anisotropic, contradicting the isotropic correction of Lam-Platzmann. Later on it was suggested by Bauer [10, 11] that inclusion

of electron-electron correlation effects may improve the theoretical difference profiles with respect to the experimental measurements. The anisotropic effects were modeled for V and Cr by introducing an energy dependent occupation function for the d-orbitals [12]. While such corrections brought the theoretical profile in better agreement with the experiment, one has to stress that this has been achieved by incorporating the corrections empirically into the calculations. Obviously, the occupation number density in the presence of the electronic correlations is non-unity below the Fermi level, the step at E_F is reduced and becomes non-zero above E_F. Kubo [13] computed the occupation number density within the GW approximation and discussed the corrections to the Compton profile for the principal directions, concluding that the strong directional differences are due to the d-bands.

In this paper we analyze the Magnetic Compton profiles obtained using the combined Density Functional and Dynamical Mean Field Theory approach for Ni and Fe. We supplement our previous results for Ni and Fe [7] by discussing magnetic Compton (MCP) profiles along the [110] and [001] directions. The comparison with the experimental data leads us to conclude that theoretical MCP spectra are improved when local correlations are taken into account. We compute also the total Compton (CP) profiles for the main three direction within the cubic symmetry ([001], [110], and [111] directions) at the LSDA and DMFT level. In addition we evaluate the second order moments of the difference of Compton profiles taken along the same momentum space direction with and without including electronic correlations:

$$\Delta J_{\mathbf{K}}(p) = J_{\mathbf{K}}^{DMFT}(p) - J_{\mathbf{K}}^{LSDA}(p). \tag{3}$$

This quantity is different from the *structural anisotropy* and its second moments $\int_0^\infty p^2 \Delta J_{\mathbf{K}}(p)$ allows us to discuss the *momentum space anisotropy of correlations effects* in Fe and Ni.

II. COMPUTATIONAL METHOD

The electronic structure calculations based on the Density Functional Theory approach were performed using the spin-polarized relativistic Korringa-Kohn-Rostoker (SPR-KKR) method in the atomic sphere approximation (ASA) [14]. The exchange-correlation potentials parametrized by Vosko, Wilk and Nusair [15] were used for the LSDA calculations. For integration over the Brillouin zone the special points method has been used [16]. In

addition to the LSDA calculations, a charge and self-energy self-consistent LSDA+DMFT scheme for correlated systems based on the KKR approach [17–19] has been used. The many-body effects are described by means of dynamical mean field theory (DMFT) [20–22] and the relativistic version of the so-called Spin-Polarized T-Matrix Fluctuation Exchange approximation [23, 24] impurity solver was used. The realistic multi-orbital interaction has been parametrized by the average screened Coulomb interaction U and the Hund exchange interaction J. The values of U and J are sometimes used as fitting parameters, although recent developments made it in principle possible to compute the dynamic electron-electron interaction matrix elements with a good accuracy [25]. The static limit of the screened energy dependent Coulomb interaction leads to a U parameter in the energy range between 2 and 4 eV for all 3d transition metals, with substantial variations associated to the choice of the local orbitals [26]. As the J parameter is not affected by screening it can be calculated directly within the LSDA and is approximately the same for all 3d elements, i.e $J \approx 0.9$ eV. In our calculations we used values for the Coulomb parameter in the range of $U = 2.0$ to 3.0 eV and the Hund exchange-interaction $J = 0.9$ eV.

The KKR Green function formalism was recently extended to compute magnetic Compton profiles (MCPs) [27–29]. In the case of a magnetic sample the spin resolved momentum densities are computed from the corresponding LSDA(+DMFT) Green functions in momentum space as:

$$n_{m_s}(\vec{p}) = -\frac{1}{\pi}\Im \int_{-\infty}^{E_F} G_{m_s}^{LDA(+DMFT)}(\vec{p},\vec{p},E)dE \ , \tag{4}$$

where $m_s =\uparrow (\downarrow)$.

The momentum density defined as $n_\uparrow(\vec{p}) + n_\downarrow(\vec{p})$ projected onto the direction $\mathbf{K}$ defined by the scattering vector, allows to define the Compton profile as a double integral in the momentum plane perpendicular to the scattering momentum $\vec{p}_z$:

$$J_{\mathbf{K}}^{LDA(+DMFT)}(p_z) = \int\int [n_\uparrow(\vec{p}) + n_\downarrow(\vec{p})]dp_x dp_y; (p_z||\mathbf{K}). \tag{5}$$

Analogously, the double integral of the spin momentum density $n_\uparrow(\vec{p}) - n_\downarrow(\vec{p})$ projected onto the scattering direction defined by the vector $\mathbf{K}$ defines the magnetic Compton profile (MCP):

$$J_{mag,\mathbf{K}}^{LDA(+DMFT)}(p_z) = \int\int [n_\uparrow(\vec{p}) - n_\downarrow(\vec{p})]dp_x dp_y; (p_z||\mathbf{K}). \tag{6}$$

The electron momentum densities are usually calculated for the principal directions $\mathbf{K} = [001], [110], [111]$ using an rectangular grid of 200 points in each direction. The maximum

value of the momentum in each direction is 8 a.u.. The Magnetic-Compton/Compton profile is normalized such that the area under its curve is equal to the magnetic moment / number of valence electrons. This means that for the ordinary Compton profile the contribution of the core electrons has been omitted, as this does not show an anisotropy.

III. ELECTRONIC CORRELATIONS IN FE AND NI

It is commonly accepted that the decisive features of ferromagnetic Fe and Ni are determined by the electronic correlation effects taking place in the relatively narrow $3d$ band, which hybridizes weakly with the $4s$ and $4p$ bands. Fe (Ni) has a cubic body (face)-centered structure with lattice parameter 2.86 (3.52) $\mathring{A}$ [30] and 8 (10) electrons within the valence band, about 7 (9) of them having predominantly d-character. Important differences between Ni and Fe are the following: Ni has a rather small exchange splitting of about $0.2 - 0.3$ eV [31–35], while in Fe this is more substantial and amounts to $2.2 - 2.4$ eV [36, 37], i.e. a difference by a factor ten. Ni exhibits a prominent satellite structure at about 6 eV below the chemical potential [38], while the existence of an analogous feature in Fe is still controversial [39]. On the other hand, Fe exhibits an "exchange splitting" persisting into the high temperature phase, while in Ni such a feature seems absent.

From a theoretical point of view, band structure calculations based on DFT are able to account for ground state properties of Fe quite reasonably. Even the most striking failure of LSDA, namely the prediction of an fcc instead of the experimental bcc ground state in Fe, is explained by the tiny energy difference between the two structures within GGA [40–43].

State-of-the art computations including many-body effects were recently used to scrutinize the paramagnetic α-phase of iron. An orbital selective local moment formation mechanism was proposed [44]. Later on Leonov et al. introduced the correlation magnetic energy and for the first time explained the α-to-γ phase transition in paramagnetic iron [45]. Subsequently this opened the path towards the computation of the phonon spectra across the α-to-γ phase transition and the study of lattice stability in the presence of electronic correlations [46]. Concerning the methodological background, the generalization to a rotational invariant exchange interaction allowed to revisit the magnetic properties of paramagnetic α iron [47] and to establish a reasonably good agreement for the Curie temperature of Fe and Ni [48]. A remarkable difference between Fe on the one side and Ni on the other side

lies in the fact that in the latter the majority spin bands are fully occupied, while this is not the case in Fe. The LSDA calculations for fcc Ni cannot reproduce some features of the electronic structure of Ni as observed experimentally. The valence band photoemission spectra of Ni shows a 3d-band width that is about 30% narrower than obtained from the LSDA calculations. It is known from VB-XPS spectra that LSDA cannot reproduce the dispersionless feature at about 6 eV binding energy (the so-called 6 eV satellite). In addition the magnetic exchange-splitting is overestimated by LSDA calculations when compared with the experimental data. An improved description of correlation effects for the 3d electrons via LSDA+DMFT gives a more correct width of the occupied 3d bands, a better exchange splitting, and also the 6 eV satellite structure in the valence band [17, 39, 49–54].

Concerning the magnetic Compton profiles of Fe and Ni, the experimental spectra and the FLAPW calculations based on LSDA are in fair agreement [55]. For Fe the center of gravity of p-states were lowered to reproduce correctly the N-centered hole pocket of the third minority-spin band [55]. This shows that LSDA needs to be supplemented to obtain a better description of the MCP. For Ni a slightly noticeable discrepancy in the spectra are seen. In the literature discrepancies between calculated and experimental MCPs are often attributed to non-local corrections to the potential stemming from electronic correlations. However, in order to check which prescription beyond the LSDA potential performs better, we first take into account local dynamic electronic correlations. Clearly, on the other hand, measurements with higher statistical accuracy are also desired, in order to provide a critical test of band theories.

A. Magnetic Compton profiles of Iron

The magnetic Compton profiles along the [111] direction for Fe and Ni including dynamic correlations were studied recently by Benea et al. [7]. Here we extend this study including results for the [001] and [110] directions for both magnetic and non-magnetic Compton profiles.

The computed magnetic Compton profiles along the [001] and [110] directions of Fe are shown in Fig. 1. The dashed (solid, red) curve represents the results of LSDA (LSDA+DMFT) calculations. The average Coulomb U=2.3 eV and exchange J=0.9 eV parameters have been used, and the temperature was taken as 400K. The experimental

MCP data are taken from the work of Sakurai et al. [56] for the [001] direction while for the [110] direction the results presented in the paper of Collins et al. [57] are given. The experimental momentum resolutions are 0.12 a.u. for the [001] and 0.7 a.u. for the [110] direction, respectively. According to this, the theoretical spectra have been convoluted with Gaussians corresponding to the experimental resolution. After convolution, the calculated MCPs have been scaled to correspond to a spin momentum of 2.3 μ_B (LSDA) and 2.19μ_B (LSDA+DMFT), respectively.

As one can see from Fig. 1 there is a fair agreement between the measured and computed MCP spectra except for the region with momenta $p_z < 2.5$ a.u. where noticeable differences are visible. The spectra change shape in the small momentum region $p_z < 2.5$ a.u., with a depletion around 1 a.u. for the [001] direction. On the other hand, for the [110] direction no such depletion is seen. In the high-momentum region $p_z > 2$ a.u., structureless similar shapes are observed for both [001] and [110] directions. Similarly to the results discussed in our recent work [7] for the [111] direction, we see that DMFT improves the agreement with the experimental spectra for the [110] direction at small momenta $p_z < 1.5$ a.u.. A different situation is noticeable for the spectra along [001]: in the vicinity of zero momentum DMFT results slightly overestimates experiment and follow very closely the LSDA data until $p_z = 1.5$ a.u.. The maxima in the LSDA profile at ≈ 1.25 a.u. is significantly reduced. However, this reduction is not sufficient to intercept the experimental data. At higher momenta both LSDA and DMFT lead to similar MCPs. Although the experimental momentum resolution is rather satisfactory, at large momenta the spread in the experimental data, in particular along [001] indicates the need for enhanced accuracy in the experiment.

To discuss further the characteristic features of the correlations we plot in Fig. 2 the difference between the total Compton profiles obtained within the LSDA- and DMFT-based calculations together with its second moment for the main three directions. A similar trend in the momentum dependence is seen.

Essentially, one can distinguish three regions: the low momentum region (I) for momentum smaller than ≈ 0.8 a.u., the intermediate region (II) 0.8 a.u.$< p_z < 2$ a.u. and finally the high momentum region $p_z > 2$ a.u. The comparison between different directions shows differences concerning the shape as well as the absolute values. The most significant discrepancies are seen at low momenta ($p_z \leq 1$ a.u.): along the [001] direction, one can find regions in which electronic correlations lead to depleted ($\Delta J < 0$) or enhanced ($\Delta J > 0$)

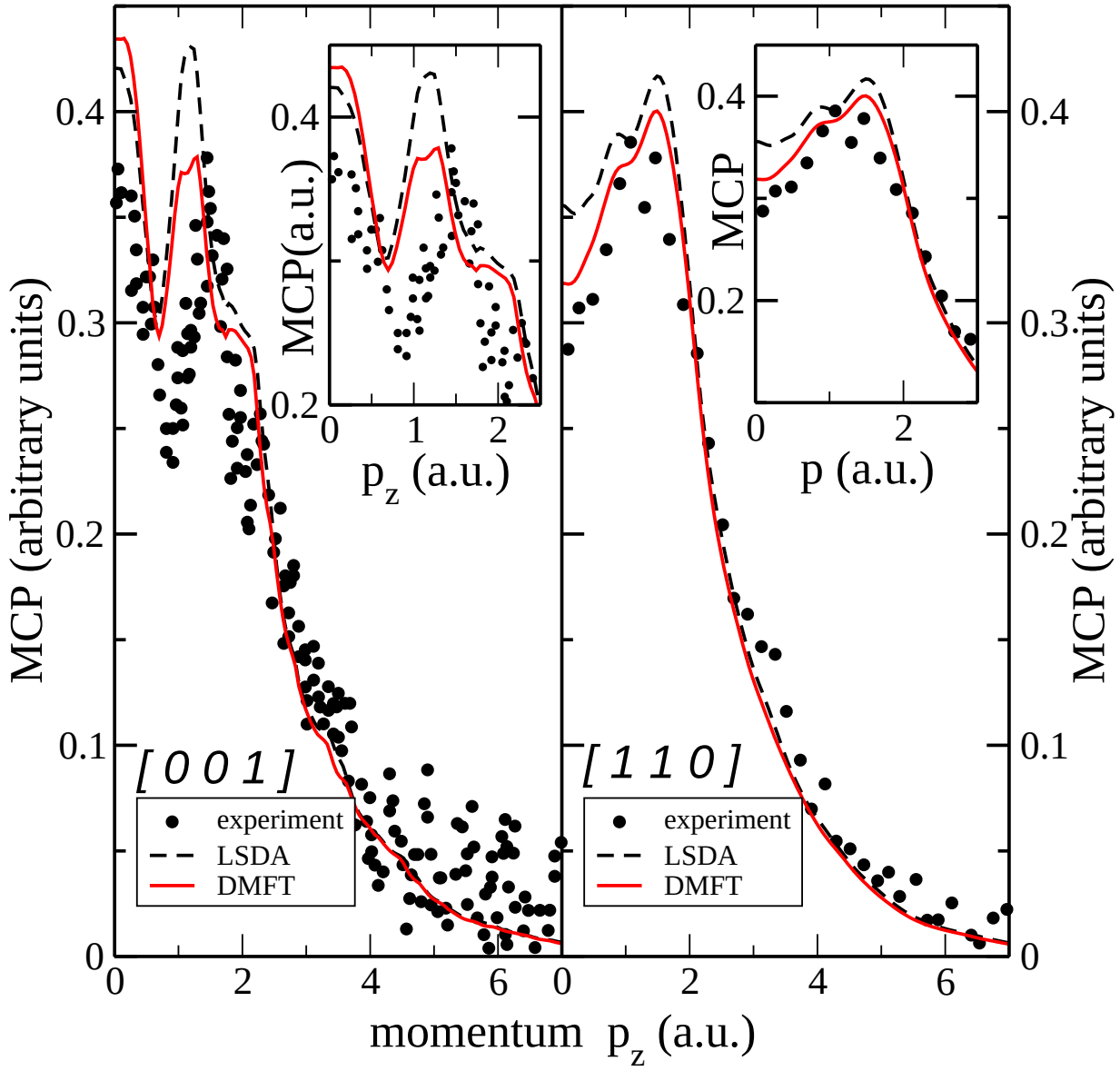

FIG. 1: (Color on-line) Magnetic Compton profiles of Fe along the [001] and [110] directions, calculated with LSDA and LSDA+DMFT with $U = 2.3$ eV, $J = 0.9$ eV and T=400K. The MCP profiles were convoluted with the experimental resolution (0.12 a.u. for [001] MCP and 0.7 a.u. for [110], respectively). The experimental MCPs stem from Sakurai et al. [56] and Collins et al. [57].

Compton profiles. In contrast to the other two [110] and [111] directions with $\Delta J > 0$ the Compton profile is enhanced because of Coulomb interactions. The maximum at $p_z = 0$ remains also along the [110] direction, while for [111], the difference ΔJ shows a peak and a central dip. Within the region of the intermediate momenta 1 a.u. $< p_z <$ 2 a.u. ΔJ has

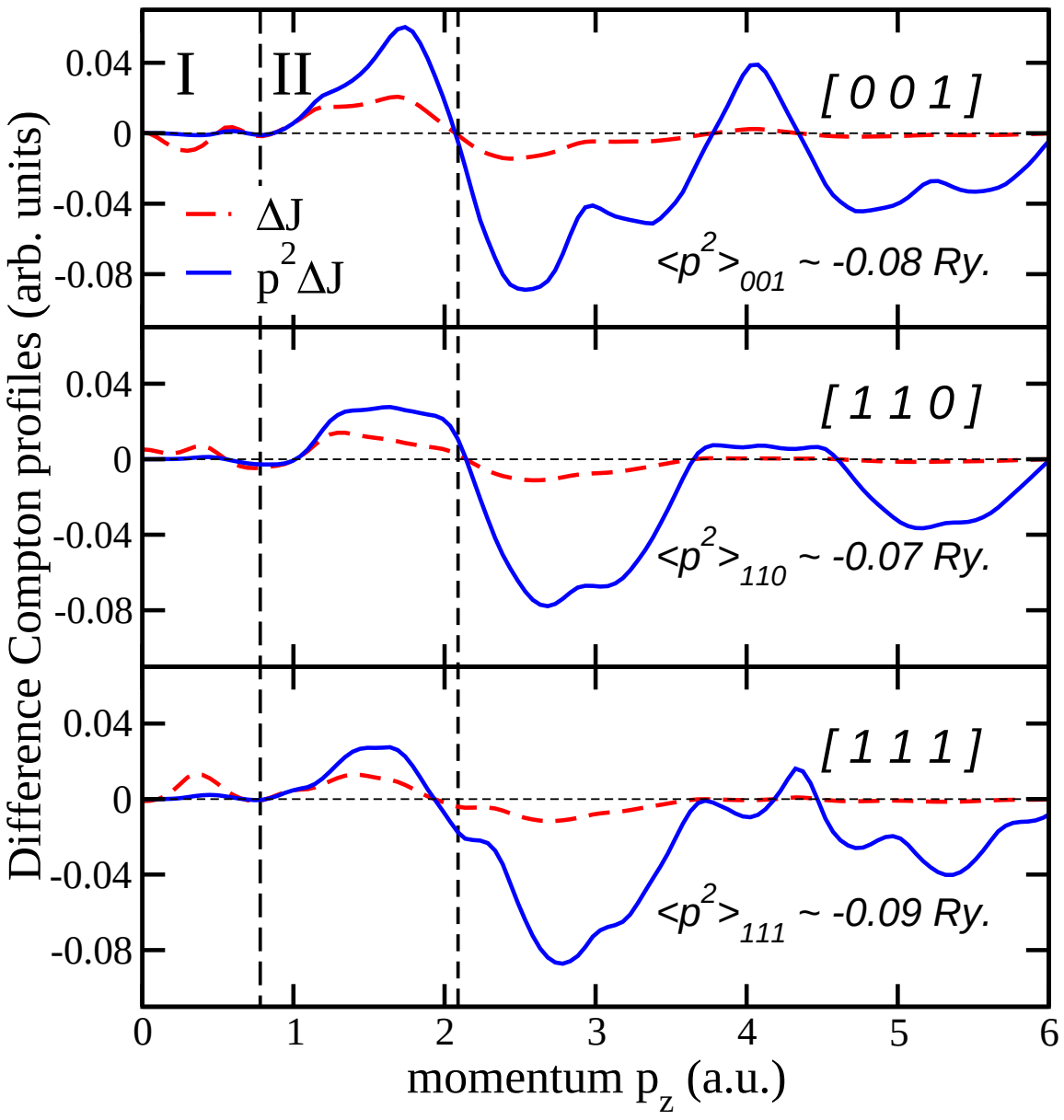

FIG. 2: (Color on-line) Differences between the LSDA+DMFT and LSDA total Compton profiles of Fe ΔJ (red dashed) and its second order moment $p^2\Delta J$ (blue solid) along [001], [110] and [111] directions. Larger values of the second moment indicate a more important electronic correlation energy contribution for the corresponding direction.

positive values along the [001] and [111] directions and small negative (around 1 a.u.) as well as positive values for [110]. Thus, the electronic correlations lead to an overall enhancement of the Compton profile in the intermediate region. For all principal directions ΔJ behave similarly in the high momentum region, being essentially negative in the entire range, with

a slightly positive hump at $p_z = 4$ a.u. for the [001] direction.

A more quantitative analysis upon the momentum space anisotropy of correlations can be made by calculating the second moment of the Compton profile. The second moment has been previously applied to study the redistributions of interatomic interactions in the momentum densities, which allowed to connect the Compton profile with the interaction energy and interatomic forces [58, 59]. Taking the second moment along the bond directions allows to study the electronic properties of the bond in momentum space. In coordinate space the charge is contracted around the nucleus and accumulated along the bond direction. The reverse of the situation happens in momentum space: momentum density is greater perpendicular to the bond direction [1]. In the same spirit, it is possible to compute the second moment of the difference between correlated and non-correlated Compton profiles, along the bond directions $\mathbf{K}$:

$$\langle p^2 \rangle_{\mathbf{K}} = \int_0^\infty p_z^2 \left[J_{\mathbf{K}}^{DMFT}(p_z) - J_{\mathbf{K}}^{LSDA}(p_z) \right] dp_z; (p_z || \mathbf{K}) \tag{7}$$

which allows to discuss the effects of the electronic interactions upon the bounded density.

In the case of Fe the values for the second moment of the difference in the total Compton profiles are given in Fig. 2. We observe that including electronic interactions treated beyond mean-field, the second moment of the difference decreases along all bonds. We have obtained a stronger decrease along the [111] and [001] direction, and weaker decrease along [110]. We note also that the decrease happens in agreement with the interatomic distances in the bcc lattice: for a shorter bond a stronger decrease is evidenced. These results demonstrate that (i) although the included interaction is only local, its consequences, i.e. the electronic correlations, show momentum space anisotropy; (ii) in addition shorter bonds experience stronger effects. A more detailed discussion concerning the connection between the second moment along a $\mathbf{K}$ direction and the energy of an interacting electronic system is provided in section Sec.III C.

B. Magnetic Compton profiles of Nickel

The magnetic Compton profiles of Ni along the [001] and [110] directions are shown in Fig. 3. The dashed (solid, red) curve represents the LSDA (LSDA+DMFT) calculations. The theoretical calculations are compared with the experimental MCP data of Dixon et al.

[60]. The experimental momentum resolution is 0.43 a.u., which was also used as Gaussian broadening parameter for the calculated MCP spectra. In addition, the calculated MCPs have been scaled to the spin magnetic moment 0.6 μ_B for LSDA and to 0.6, 0.57, 0.56 and 0.5 μ_B for the corresponding values of U = 1.8, 2.0, 2.3 and 3.0 eV for the LSDA+DMFT calculations.

As one can see in Fig. 3 (upper panel) LSDA results are already in reasonable agreement with the measurements. They capture the behavior at large moments, get close to the maximum at $\approx$ 1.8 a.u. and overestimate the contributions in the low momentum region. Dixon et al. [60] analyzed the magnetic Compton profile of Ni comparing LSDA and GGA results obtained through a linear muffin-tin orbitals (LMTO) method. In their theory, and in particular from the analysis of the fifth band, Dixon et al. [60] identified several main peaks, which they labeled from A until G. In the present study all these major features are essentially reproduced, although they are not very evident in our plot, due to the Gaussian broadening. The first two peaks, which LSDA locates at 0.3/0.7 a.u (inside the first Brillouin zone), are not resolved by the experiment. The highest peaks, labeled as C and D, are located at 1.25/1.70 a.u., and are followed by other Umklapp peaks at 2.7 (E), 3.6 a.u (F) and a further shoulder at G. The LSDA results (dashed black line) overestimates significantly the contributions in the low momentum region, while the DMFT profile is in much better agreement with experiments, until the peak D. There are no essential differences between the LSDA and LSDA+DMFT spectra for momenta larger than $\approx$ 1.7 a.u..

The lower panel of Fig. 3, shows the MCPs along the [110] direction. As for the [001] direction, our results are in good agreement with previous results by Dixon et al. [60]. Following their notation, a first peak A is situated inside the first Brillouin zone, and located around 0.7 a.u.. All subsequent peaks are essentially of Umklapp origin, and the maximum of the MCP is at C, being overestimated in theory in comparison with experiment. It was remarked by Dixon et al. [60] that all computed peaks at higher momenta E (3.3 a.u) and F (4.7 a.u.) are more visible than the corresponding maxima in the experiment. This seems to hold also for DMFT results. Instead, the low momentum region ($p_z < 1.7$ a.u.) is in better agreement with experiment, in particular for the value at zero momentum and for the peak within the first Brillouin zone (A). Further, the experimental value of the MCP at B seems to be at an intermediate level between LSDA and DMFT. Both LSDA and DMFT overestimate the maximum C from where they follow a very similar momentum dependence,

as mentioned above.

The MCP for Ni along the [001] direction using LSDA and LSDA+DMFT are presented in Fig. 4 for different values of the U parameter. The experimental data are shown with dots and the LSDA results are given by dashed lines. The DMFT results are presented for U = 1.8, 2.0, 2.3 and 3.0 eV and are respectively plotted with green (dot-dashed), blue (dot-dot-dashed), red (solid) and violet (dashed-dot-dashed) lines. The values in the region of low momentum, up to $p_z < 1$ a.u. (most of it in the first Brillouin zone), are better captured by the intermediate values of U = 2.3 eV. A slightly over- and a more significant underestimation can be noticed for 2.0 eV and 3.0 eV, respectively. Around the maximum ($p_z \approx 1.7$ a.u.) of the experimental profile (label D) LSDA and all DMFT results U =1.8, 2.0 and 2.3 eV overestimate the magnitude of the maxima, except U=3 eV which underestimates the contribution at this position. For momenta larger than point D the DMFT profiles with U = 2.0 and 2.3 eV and the LSDA profile have essentially the same behavior, in good agreement with experimental data. Dixon et al. [60] noted that discrepancies may not be eliminated simply renormalizing the magnetic moment because the moment is connected to the exchange splitting, therefore this would not necessarily scale the MCP spectra. Figs. 3 and Fig. 4 show that electronic correlations beyond LSDA/GGA improve the spectra in the low momentum region. We mentioned above (Sec. III) that the reduction of exchange splitting is one among several subtle consequences of the correlation effects in Ni/Fe. Therefore DMFT accounts naturally for the renormalization, in this case the reduction of the magnetic moment. Obviously, this has consequences on the entire momentum dependence of the MCP spectrum, also in the high momentum region. The high momentum behavior was attributed to a free-atom type profile [61], based on the argument that the strong weighting of the high momentum components into the sum of the second moments dominates the cohesive energy. This argument may be invoked also in the presence of electronic correlations, although the non-interacting and interacting case have different atomic-limits. As Figs. 3 and 4 show in the high momentum region very similar LSDA and DMFT profiles, electronic correlations seem to have little influence in this region. To learn more about the consequence of electronic correlations in the following we analyze the difference of the total Compton profiles with and without correlations and its second order moments.

In Fig. 5 the difference between the LSDA and DMFT total Compton profiles ΔJ is

shown together with its second order moment $p^2\Delta J$. The theoretical CP profiles were broadened with a Gaussian of 0.22 a.u. width. The momentum dependence of $p^2\Delta J(p)$ and the second moments of the difference Compton profiles are depicted in Fig. 5 along [001] and in Fig. 5 for the [110] and [111] directions. For all principal directions the weight of $p^2J^{DMFT}(p) > p^2J^{LSDA}(p)$ for moments $p_z < 2$ a.u., while for larger moments $p^2\Delta J(p)$ has a negative weight. This shows that the DMFT derived correlation is significant in the low momentum region, $p_z < 2$ a.u.. This result allows to extend the concept of spectral weight transfer from real space into momentum space. In the real space representation spectral weight transfer is discussed in terms of the changes of the spectral properties as a function of the strength of the local interaction, U. For larger U values, spectral weight is redistributed form the Fermi level towards high binding energies. In momentum space more states/electrons are transferred towards low energies for small momenta $p_z < 2$ a.u., while at large values of p spectral weight is shifted towards high momentum region.

Along the [001] direction the spectra have mostly a negative weight, and the estimated values for the second moments are -0.05 Ry for $U = 2$ eV, -0.07 Ry for $U = 2.3$ eV and -0.15 Ry for $U = 3.0$ eV. One notices that larger values of U determine larger values (in absolute terms) of the second moment, although the precise increase of these values is different along different directions. Along the [110] direction the magnitude of the second moment is similar being -0.04, -0.06, -0.12 Ry, while along [111] smaller values for the second moments are obtained.

C. Discussions and Conclusion

The Compton scattering experiment yields the one-dimensional momentum distribution for the scatterer. Therefore, it is possible to use Compton data to calculate the expectation values of operators which are functions of momentum $\langle p^n \rangle$. The value for $n = 2$ is of special interest, since $1/2\langle p^n \rangle$ gives the electronic kinetic energy, leading to a connection with the total energy of the scattering system. As a result, the computed Compton profile can be easily interpreted as a very fundamental quantity. In the following we discuss the connection between the second moment of the difference between correlated (LSDA+DMFT) and non-correlated (LSDA) Compton profiles and the kinetic energy of the electronic system. Our

main focus is on the bond average of the second moment of the difference Compton profiles:

$$\overline{\langle p^2 \rangle} = \frac{1}{N_b} \sum_{\mathbf{K}} \int_0^\infty p_z^2 \Delta J_{\mathbf{K}}(p_z) dp_z \propto E_{kin}^{DMFT} - E_{kin}^{LSDA}. \tag{8}$$

Here the overbar represents the average taken over the bonds extended along the **K**-directions, $\Delta J_{\mathbf{K}}(p_z)$ is the difference of total Compton profile, N_b is the number of bonds and the energies on the right hand side are the kinetic energies computed in DMFT/LSDA. In general, calculating total energies in LSDA+DMFT is a difficult task, and requires the evaluation of an energy functional with several terms [18, 62] including the Galitskii-Migdal contribution [63], i.e. $1/2\mathrm{Tr}[\hat{\Sigma}\hat{G}]$, and the double counting as well. The LSDA+DMFT total energy functional can in principle be analyzed to obtain an expression for the kinetic energy similarly to what is done for DFT [64, 65]. When focusing on the differences between LSDA+DMFT and LSDA, one can write:

$$\begin{aligned} \Delta E_{kin} =& \mathrm{Tr}\left[\hat{H}_{KS}^{DMFT}\hat{G}^{DMFT}\right] - \\ & \mathrm{Tr}\left[\hat{H}_{KS}^{LSDA}\hat{G}^{LSDA}\right] + \langle \Delta V_{KS} \rangle + \langle \Delta T_c \rangle. \end{aligned} \tag{9}$$

In this expression the first and second terms on the right hand side are the single particle energies of the Kohn-Sham Hamiltonian within LSDA+DMFT and LSDA, while the third term is the expectation value of the difference of their corresponding Kohn-Sham potentials. The last term in Eq. (9) is the variation of the exchange-correlation contribution to the kinetic energy, and can in principle be expressed in terms of the exchange-correlation potential and its gradient [65].

In spite of the recent progress in improving the accuracy of LDA+DMFT energetics [18, 62] it is still a difficult task to compute not only LSDA+DMFT total energies but also the terms in discussion with a high degree of accuracy. In addition, the energy components given in Eq. (9) being complete traces, would not provide any information about the magnitude of the correlation energy along different bonds or directions in the **k**-space. On contrary, the analysis of the second moments along the bonds $\langle p^2 \rangle_{\mathbf{K}}$ as shown in Figs. 2, 5 and 6 demonstrates that changes in the kinetic energy because of electronic correlations are anisotropic. One has to note that the main source for the anisotropy in the momentum space is bond directionality that is already captured within the LSDA. However this can not provide any measure of the electronic correlations.

In Fig. 7 we show the second moment of the difference $\Delta J_{\mathbf{K}}(p)$ along the principal directions and its directional average. The latter is estimated as the weighted sum of the nearest neighbors i.e. six times the contribution along [001], 12 times the contribution along [110] and 8 times the contribution along [111] divided by the total number of neighbors (26). The values of the second moments are almost similar along [110] and [001] directions and smaller than along [111] direction. For sake of comparison, in Fig. 7 we also show the variation of the kinetic energy as obtained from Eq. (9) by ignoring the last term $\langle \Delta T_c \rangle$. These data were obtained through a full-potential linearized muffin-tin orbital (FP-LMTO) code [39, 53], which has been shown to give results in very good agreement with SPR-KKR regarding LSDA+DMFT total energies [18]. Due to the aforementioned approximations and a very high sensitivity to the numerical and computational details, any quantitative comparison between second moment of $\Delta J_{\mathbf{K}}(p)$ from SPR-KKR and ΔE_{kin} from FP-LMTO is problematic. In fact, from Fig. 7, it is clear that the two contributions are still far from a quantitative agreement. However, we capture a consistent qualitative picture pointing to a decrease of kinetic energy difference for increasing U. It is important to note that the second moment of the Compton profile turns out to be negative because the positive contribution in the low momentum region up to $p_z < 2$ a.u., is completely overruled by the large negative contribution from high momenta. In the low momentum region increasing the values of U an increasing in the kinetic energy is obtained, which is in agreement with the argument that the presence of U penalizes the electrons and leads to an increase in their kinetic energy. This argument is not valid any more in the region of high momenta, where the mean-field type exchange-correlation dominates the "Hubbard-U" contribution. Further analysis is needed in order to make a more quantitative comparison, especially to understand the role of the double counting correction and the effects of the expectation value of T_c, discarded in the present analysis.

Concerning the charge redistribution in Ni, the real space picture corresponds to the contraction of the electronic charge because of correlation effects, as seen from previous coordinate space charge computation [50]. The overall negative second moment of the difference tells us that the corresponding kinetic energy is decreasing with increasing the strength of U. Therefore, the less mobile correlated d-electrons would weaken the covalent component of the metallic bonding seen in transition metals. In addition as one can see in Fig. 7, this effect is anisotropic. Similarly for Fe the covalent d-d contribution is weakened as well in the

presence of correlations. In comparison to Fe, Ni shows larger values of the second moments $p^2\Delta J$ along [001] and [110], while for the [111] direction the opposite situation is found. This is an expected result as the shortest distance and the strongest bond is realized along the [111] direction, of the bcc-structure. As a common feature both Fe and Ni show positive values for $\Delta J_{\mathbf{K}}(p)$ and consequently positive second order moments up to the $p_z < 2$ a.u. momenta. This value seems to be the upper bound in the momentum space up to which many-body correlation effects captured by DMFT have a larger weight in comparison to the exchange and correlation effects described by LSDA.

To conclude, in the present work we studied the influence of electronic correlations on the Compton profiles of Fe and Ni within the framework of density functional theory using the LSDA+DMFT approach. The second moment of the Compton profile difference allows to quantify the momentum space anisotropy of the electronic correlations of Fe and Ni. The changes in the shape and magnitude of the anisotropy have been discussed as a function of the strength of the Coulomb interaction U. According to our results Ni has a larger momentum space anisotropy of the second moment of the total Compton profile in comparison with Fe. In the range of the studied values of U no significant dependence is seen in the anisotropy of the Compton profile. As an overall conclusion DMFT introduces moderate improvements for the spectral features in particular at low momentum. Further progress is needed to bridge between momentum density and the total energy of the system through the computed Compton profile.

IV. ACKNOWLEDGMENTS

This research was supported in part by the Deutsche Forschungsgemeinschaft through FOR 1346. DAAD and the CNCS - UEFISCDI (project number PN-II-ID-PCE-2012-4-0470) are gratefully acknowledged. D. B would like to express a deep gratitude to Prof. V. Crişan (UBB Cluj, Romania) for his support and encouragement during her study period and early career. I. D. M acknowledges the Swedish National Infrastructure for Computing (SNIC) for providing computational resources at the National Supercomputer Center (NSC).

L. C. acknowledge the discussions with I. Leonov.

[1] M. J. Cooper, Rep. Prog. Phys. **48**, 415 (1985).

[2] S. Wakoh and Y. Kubo, J. Magn. Magn. Materials **5**, 202 (1977).

[3] T. Baruah, R. R. Zope, and A. Kshirsagar, Phys. Rev. B **62**, 16435 (2000).

[4] M. Tokii and M. Matsumoto, J. Phys.: Condensed Matter **18**, 3639 (2006).

[5] Y. Kubo, J. Phys. Chem. Solids **65**, 2077 (2004).

[6] J. Rath, C. S. Wang, R. A. Tawil, and J. Callaway, Phys. Rev. B **8**, 5139 (1973).

[7] D. Benea, J. Minár, L. Chioncel, S. Mankovsky, and H. Ebert, Phys. Rev. B **85**, 085109 (2012).

[8] L. Lam and P. M. Platzman, Phys. Rev. B **9**, 5122 (1974).

[9] L. Lam and P. M. Platzman, Phys. Rev. B **9**, 5128 (1974).

[10] G. E. W. Bauer and J. R. Schneider, Z. Physik B **54**, 17 (1983).

[11] G. E. W. Bauer, Phys. Rev. B **30**, 1010 (1984).

[12] S. Wakoh and M. Matsumoto, J. Phys.: Condensed Matter **2**, 797 (1990).

[13] Y. Kubo, J. Phys. Chem. Solids **62**, 2199 (2001), ISSN 0022-3697.

[14] H. Ebert, D. Ködderitzsch, and J. Minár, Rep. Prog. Phys. **74**, 096501 (2011).

[15] S. H. Vosko, L. Wilk, and M. Nusair, Can. J. Phys. **58**, 1200 (1980).

[16] H. J. Monkhorst and J. D. Pack, Phys. Rev. B **13**, 5188 (1976).

[17] J. Minár, L. Chioncel, A. Perlov, H. Ebert, M. I. Katsnelson, and A. I. Lichtenstein, Phys. Rev. B **72**, 045125 (2005).

[18] I. D. Marco, J. Minár, S. Chadov, M. I. Katsnelson, H. Ebert, and A. I. Lichtenstein, Phys. Rev. B **79**, 115111 (2009).

[19] J. Minár, J. Phys.: Condensed Matter **23**, 253201 (2011).

[20] W. Metzner and D. Vollhardt, Phys. Rev. Letters **62**, 324 (1989).

[21] A. Georges, G. Kotliar, W. Krauth, and M. J. Rozenberg, Rev. Mod. Phys. **68**, 13 (1996).

[22] G. Kotliar and D. Vollhardt, Phys. Today **57**, 53 (2004).

[23] M. I. Katsnelson and A. I. Lichtenstein, Eur. Phys. J. B (2002).

[24] L. V. Pourovskii, M. I. Katsnelson, and A. I. Lichtenstein, Phys. Rev. B (2005).

[25] F. Aryasetiawan, M. Imada, A. Georges, G. Kotliar, S. Biermann, and A. I. Lichtenstein,

Phys. Rev. B **70**, 195104 (2004).

[26] T. Miyake and F. Aryasetiawan, Phys. Rev. B **77**, 085122 (2008).

[27] Z. Szotek, B. L. Gyorffy, G. M. Stocks, and W. M. Temmerman, J. Phys. F: Met. Phys. **14**, 2571 (1984).

[28] D. Benea, S. Mankovsky, and H. Ebert, Phys. Rev. B **73**, 094411 (2006).

[29] D. Benea, Ph.D. thesis, LMU München (2004).

[30] T. C. Leung, C. T. Chan, and B. N. Harmon, Phys. Rev. B **44**, 2923 (1991).

[31] D. E. Eastman, F. J. Himpsel, and J. A. Knapp, Phys. Rev. Lett. **40**, 1514 (1978).

[32] E. Dietz, U. Gerhardt, and C. J. Maetz, Phys. Rev. Lett. **40**, 892 (1978).

[33] F. J. Himpsel, J. A. Knapp, and D. E. Eastman, Phys. Rev. B **19**, 2919 (1979).

[34] D. E. Eastman, F. J. Himpsel, and J. A. Knapp, Phys. Rev. Lett. **44**, 95 (1980).

[35] W. Eberhardt and E. W. Plummer, Phys. Rev. B **21**, 3245 (1980).

[36] E. Kisker, K. Schröder, W. Gudat, and M. Campagna, Phys. Rev. B **31**, 329 (1985).

[37] J. Kirschner, M. Glöbl, V. Dose, and H. Scheidt, Phys. Rev. Lett. **53**, 612 (1984).

[38] C. Guillot, Y. Bally, J. Paigné, J. Lecante, K. P. Jain, P. Thiry, R. Pinchaux, Y. Petroff, and L. M. Falicov, Phys. Rev. Letters **39**, 1632 (1977).

[39] A. Grechnev, I. D. Marco, M. I. Katsnelson, A. I. Lichtenstein, J. Wills, and O. Eriksson, Phys. Rev. B **76**, 035107 (2007).

[40] P. Bagno, O. Jepsen, and O. Gunnarsson, Phys. Rev. B **40**, 1997 (1989).

[41] B. Barbiellini, E. G. Moroni, and T. Jarlborg, J. Phys.: Condensed Matter **2**, 7597 (1990).

[42] J. M. MacLaren, D. P. Clougherty, and R. C. Albers, Phys. Rev. B **42**, 3205 (1990).

[43] D. J. Singh, W. E. Pickett, and H. Krakauer, Phys. Rev. B **43**, 11628 (1991).

[44] A. A. Katanin, A. I. Poteryaev, A. V. Efremov, A. O. Shorikov, S. L. Skornyakov, M. A. Korotin, and V. I. Anisimov, Phys. Rev. B **81**, 045117 (2010).

[45] I. Leonov, A. I. Poteryaev, V. I. Anisimov, and D. Vollahrdt, Phys. Rev. Letters **106**, 106405 (2011).

[46] I. Leonov, A. I. Poteryaev, V. I. Anisimov, and D. Vollahrdt, Phys. Rev. B **85**, 020401 (2012).

[47] V. I. Anisomov, A. S. Belozerov, A. I. Poteryaev, and I. Leonov, Phys. Rev. B **86**, 035152 (2012).

[48] A. S. Belozerov, I. Leonov, and V. I. Anisomov, Phys. Rev. B **87**, 125138 (2013).

[49] A. I. Lichtenstein, M. I. Katsnelson, and G. Kotliar, Phys. Rev. Letters **87**, 067205 (2001).

[50] L. Chioncel, L. Vitos, I. A. Abrikosov, J. Kollár, M. I. Katsnelson, and A. I. Lichtenstein, Phys. Rev. B **67**, 235106 (2003).

[51] J. Braun, J. Minár, H. Ebert, M. I. Katsnelson, and A. I. Lichtenstein, Phys. Rev. Lett. **97**, 227601 (2006).

[52] J. Sánchez-Barriga, J. Fink, V. Boni, I. Di Marco, J. Braun, J. Minár, A. Varykhalov, O. Rader, V. Bellini, F. Manghi, et al., Phys. Rev. Lett. **103**, 267203 (2009).

[53] O. Granas, I. di Marco, P. Thunström, L. Nordström, O. Eriksson, T. Björkman, and J. Wills, Comp. Mat. Sci. **55**, 295 (2012).

[54] J. Sánchez-Barriga, J. Braun, J. Minár, I. Di Marco, A. Varykhalov, O. Rader, V. Boni, V. Bellini, F. Manghi, H. Ebert, et al., Phys. Rev. B **85**, 205109 (2012).

[55] Y. Kubo and S. Asano, Phys. Rev. B **42**, 4431 (1990).

[56] Y. Sakurai, Y. Tanaka, T. Ohata, Y. Watanabe, S. Nanao, Y. Ushigami, T. Iwazumi, H. Kawata, and N. Shiotani, J. Phys.: Condensed Matter **6**, 9469 (1994).

[57] S. P. Collins, M. J. Cooper, D. Timms, A. Brahmia, D. Laundy, and P. Kane, J. Phys.: Condensed Matter **1**, 9009 (1989).

[58] T. Koga and M. Morita, Theoret. Chim. Acta. (Berlin) **61**, 73 (1982).

[59] A. J. Thakkar, Intern. J. Quantum. Chem. **23**, 227 (1983).

[60] M. A. G. Dixon, J. A. Duffy, S. Gardelis, J. E. McCarthy, M. J. Cooper, S. B. Dugdale, T. Jarlborg, and D. N. Timms, J. Phys.: Condensed Matter **10**, 2759 (1998).

[61] M. J. Cooper and J. A. Duffy, J. Phys. Chem. Solids **61**, 345 (2000).

[62] G. Kotliar, S. Y. Savrasov, K. Haule, V. S. Oudovenko, O. Parcollet, and C. A. Marianetti, Rev. Mod. Phys. **78**, 865 (2006).

[63] V. M. Galitskii and A. B. Migdal, Sov. Phys. J.E.T.P. **7**, 96 (1958).

[64] M. Levy and J. P. Perdew, Phys. Rev. A **32**, 2010 (1985).

[65] J. I. Rodríguez, P. W. Ayers, A. W. Götz, and F. L. Castillo-Alvarado, The Journal of Chemical Physics **131**, 021101 (2009).

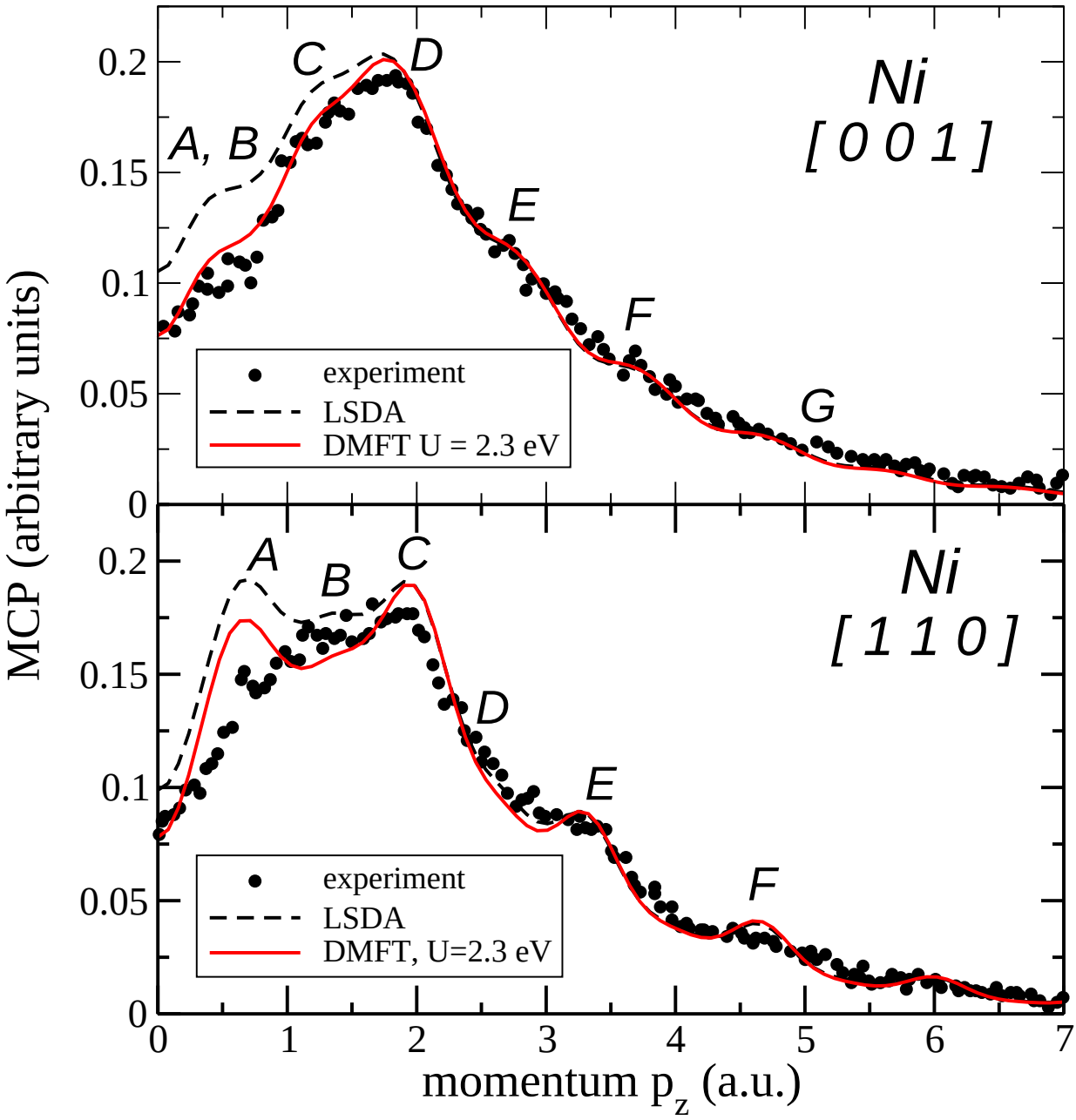

FIG. 3: (Color on-line) Magnetic Compton profiles of Ni along [001] (upper panel) and [110] (lower panel) directions, computed with LSDA and LSDA+DMFT with $U = 2.3$ eV, $J = 0.9$ eV and T=400K. The computed data were convoluted according to the experimental resolution of 0.43 a.u.. The experimental profiles are taken from Ref. [60].

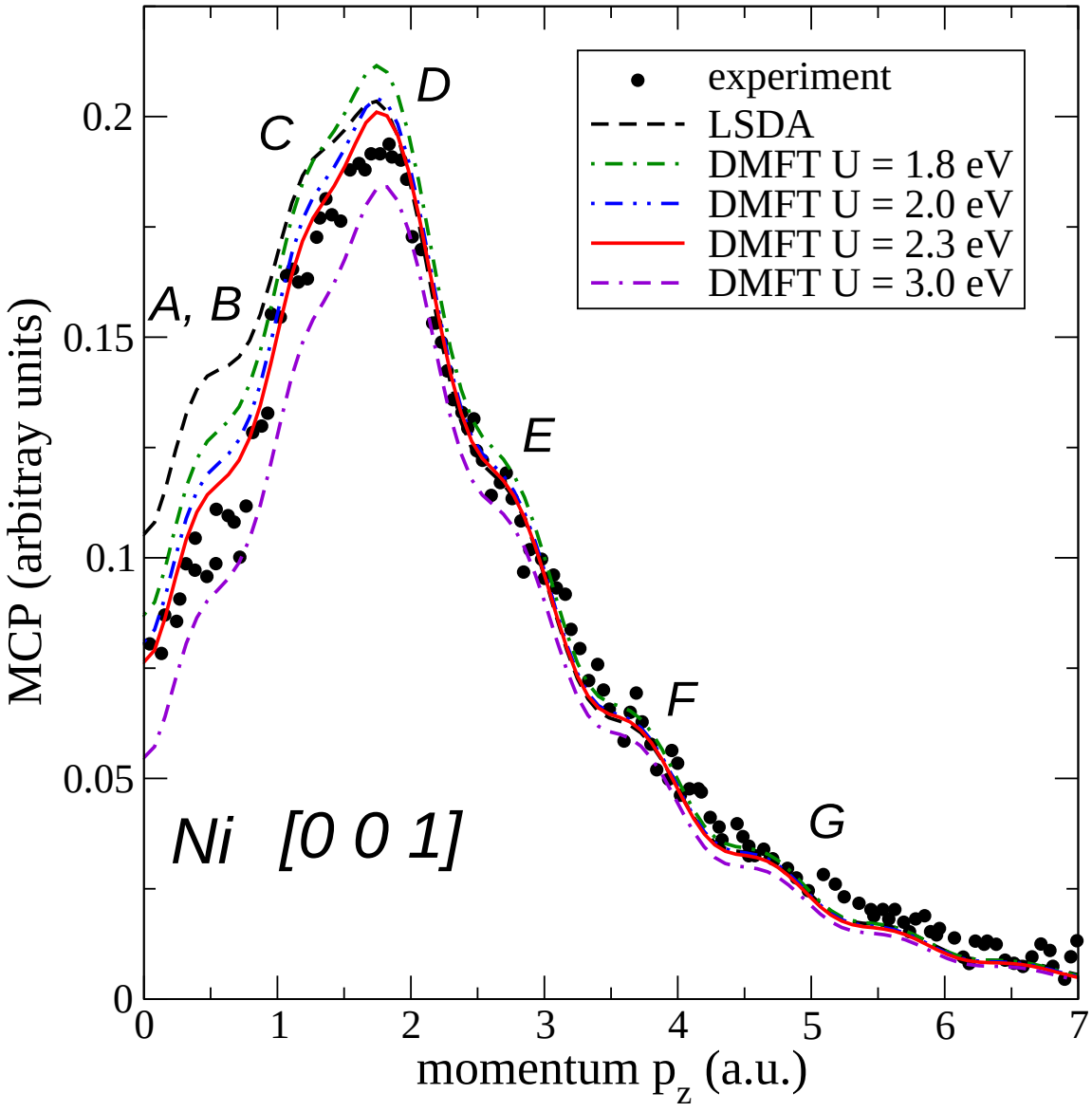

FIG. 4: (Color on-line) Magnetic Compton profiles of Ni along [001] direction. Black dashed-solid LSDA, red solid-line LSDA+DMFT for $U = 2.3$ eV, dot-dashed-blue line $U = 2.0$ eV and dot-dot-dashed $U = 3.0$ eV. In all calculations $J = 0.9$ eV and T=400K. The experimental data is taken from Ref. [60] (momentum resolution 0.43 a.u.).

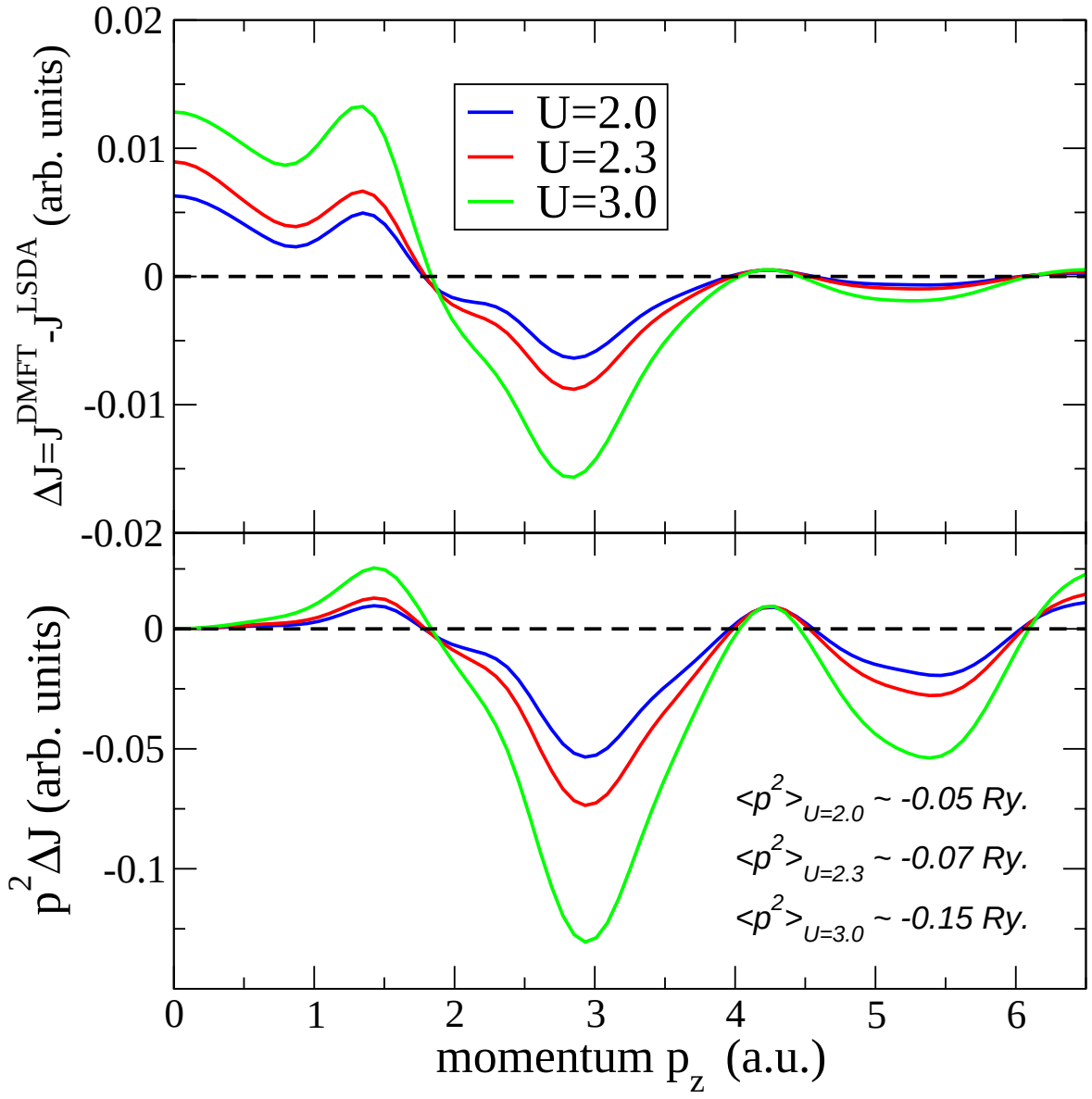

FIG. 5: (Color on-line) Difference of the Compton profile (top) and $p^2\Delta J$ (bottom), together with the second moments. Values for the second moments are given in Ry.

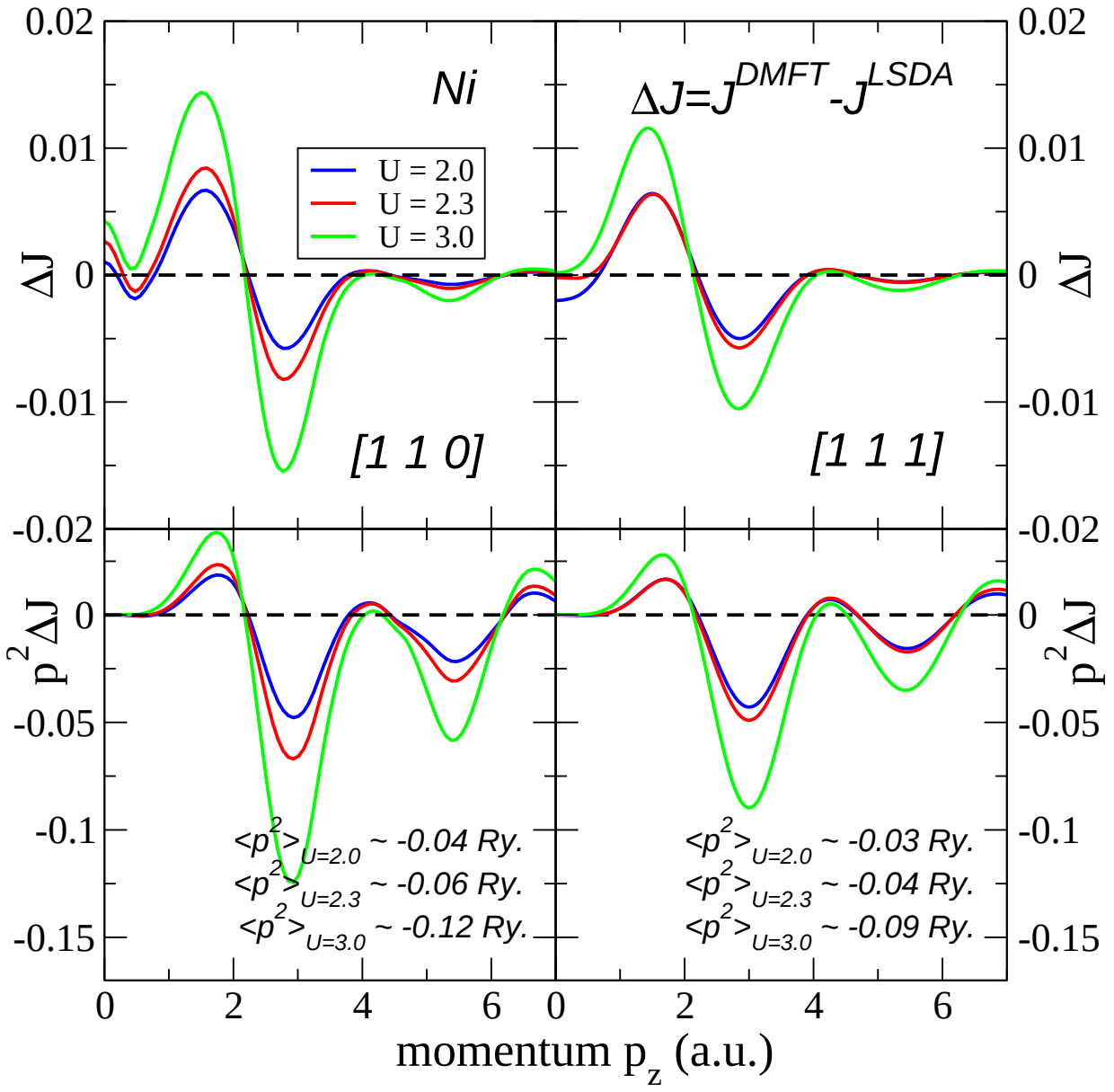

FIG. 6: (Color on-line) Differences between the LSDA and LSDA+DMFT total Compton profiles of Ni along the [110] (left column) and [111] (right column) directions for different values of U. The values of the second moment are larger along the [110] direction at all values of U.

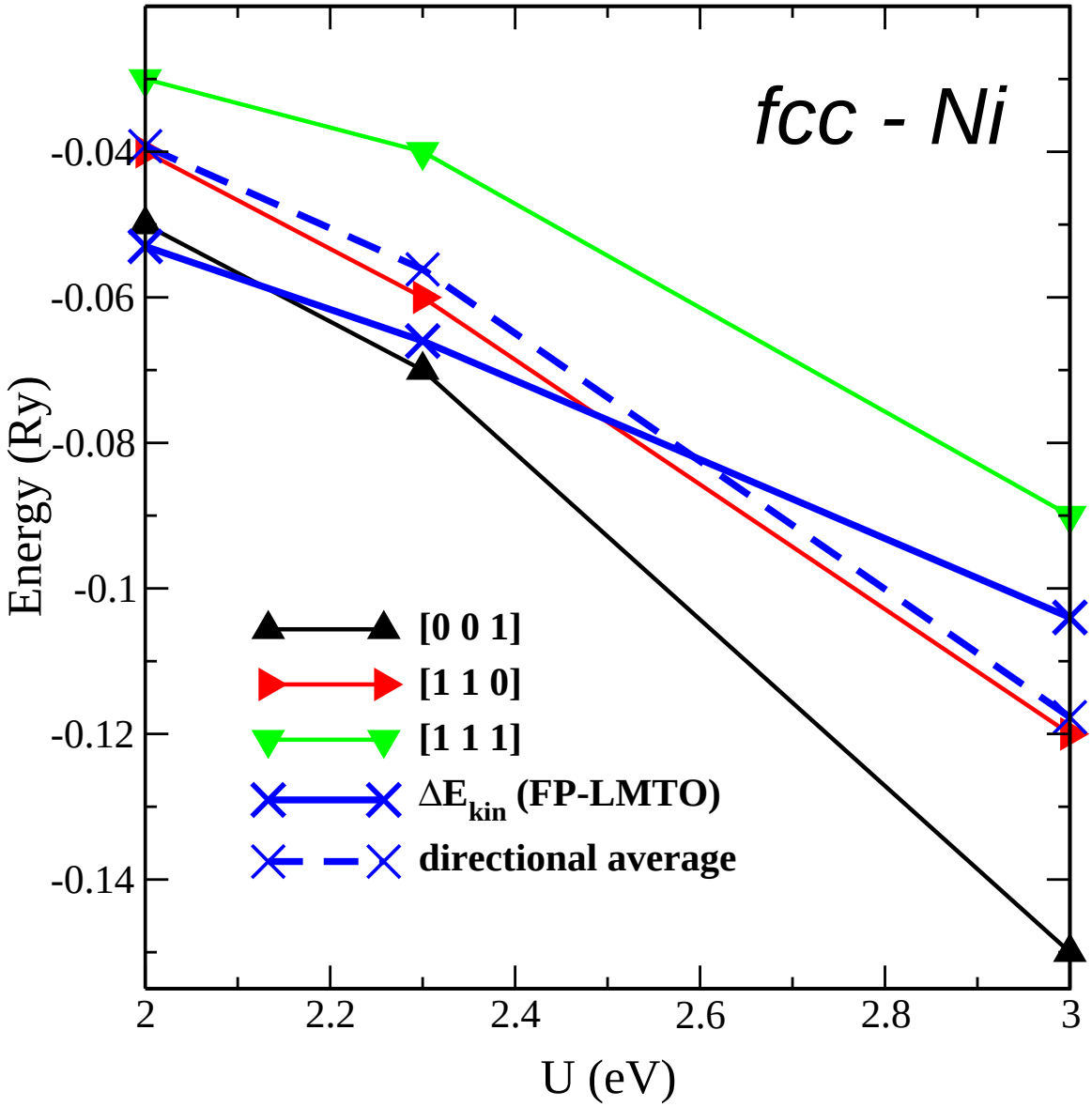

FIG. 7: (Color on-line) Second moment of the difference $\Delta J_{\mathbf{K}}(p)$ along the directions [001] (solid black line with triangles up), [110] (solid red line with triangles right), and [111] (solid green line with triangles down), together with the directional average over the bonds (dashed blue line with crosses). Moreover the approximate difference in kinetic energy between LSDA+DMFT and LSDA as obtained by FP-LMTO [39, 53] is also shown.